5-2016

Modeling and Experimental Investigation on the Influence of Radiation Defects on Helium Behavior in BCC Iron

Zuya Huang
University of Tennessee - Knoxville, zhuang18@vols.utk.edu

To the Graduate Council:

I am submitting herewith a thesis written by Zuya Huang entitled "Modeling and Experimental Investigation on the Influence of Radiation Defects on Helium Behavior in BCC Iron." I have examined the final electronic copy of this thesis for form and content and recommend that it be accepted in partial fulfillment of the requirements for the degree of Master of Science, with a major in Nuclear Engineering.

Brian D. Wirth, Major Professor

We have read this thesis and recommend its acceptance:

Steven J. Zinkle, Maik K. Lang

Accepted for the Council:
Carolyn R. Hodges

Vice Provost and Dean of the Graduate School

(Original signatures are on file with official student records.)

Modeling and Experimental Investigation on the Influence of Radiation Defects on Helium Behavior in BCC Iron

A Thesis Presented for the
Master of Science
Degree
The University of Tennessee, Knoxville

Zuya Huang

May 2016

Acknowledgements

My family

My devoted advisor Brian D. Wirth and Dr. Xunxiang Hu

Abstract

Fe-based alloys are important structural materials for both fission and fusion energy. For fusion applications, the challenges of radiation-induced changes in microstructure, properties and performance is further challenged by the concomitant production of helium from (n, alpha) nuclear reactions and fusion reactions. Due to the lack of a volumetric, high flux 14-MeV neutron source, studying these phenomena require the use of computational materials modeling and novel experimental methods. In this thesis, molecular dynamics (MD) simulations was used to investigate the synergistic interactions of helium with prismatic dislocation loops characteristic of those observed in neutron irradiated iron to determine how the presence of these loops modify the helium clustering and gas bubble nucleation process. In particular, multiple MD simulations have been conducted to investigate the role of a/2<111> or a<100> prismatic interstitial type dislocation loops on the helium clustering dynamics upon inserting interstitial helium into the body-centered cubic iron lattice at temperatures from 773 °K to 1173 °K. The simulations indicate a strong elastic interaction, which significantly influences the early stages of helium clustering that can aid bubble nucleation.

In addition, helium interactions with defect clusters in iron are probed experimentally, which has specifically focused on performing low energy helium ion implantation on neutron irradiated iron specimens followed by thermal desorption spectroscopy (TDS). The results show a limited increase in the dislocation line density, along with a relatively low volume fraction of cavities is observed after neutron irradiation of both single crystal and poly-crystalline iron samples. The TDS results indicate that the major helium desorption peaks shift to higher temperature due to the existence of the radiation induced defects, which are believed to act as strong trapping sites for helium.

Overall, the research performed in this thesis has confirmed that synergistic interactions occur between helium and point defect clusters, as well as the potential to combine computational modeling with experimental measurements using thermal desorption spectroscopy. The presented simulation and experimental results along with

the proposed future work are expected to enhance the current understanding of the fundamentals of helium-defect interactions in neutron-irradiated iron.

Table of Contents

List of Tables

List of Figures

Chapter 1

Introduction and motivation

1.1 Materials challenges in nuclear environment

1.1.1 Background

The environmental consequence of power generation is becoming more broadly recognized, which is increasing the emphasis on nuclear power as a promising clean and safe energy source. Global population growth in combination with industrial development will lead to a doubling of electricity consumption by 2030. Climate change has also been raised as an urgent problem for society. Fossil fuel will need to be replaced by low-emission source such as nuclear energy, which has demonstrated capability as the most cost-efficient of the available base-load technologies [1-5].

Nuclear energy can be divided into two categories. One is fission, which is considered as an increasingly reliable supplier of base-load electricity, as it is widely used throughout the world. The other is fusion, which is a potentially attractive, but technologically challenging endeavor and has been ranked by the US National Academy of Engineering as one of the top engineering grand challenges of the 21st century [6]. The operating environment for materials in current and proposed future nuclear energy systems is extremely harsh. The challenging fusion reactor environment (radiation, heat flux, chemical compatibility, thermomechanical stresses) will require utilization of advanced structural materials in order to fulfill the promise of fusion energy to provide safe, economical, and environmentally acceptable energy [7].

In the current and next generation of water-cooled fission reactors, corrosion and stress corrosion crack of structural materials and neutron-induced embrittlement of reactor pressure vessels are the three main degradation issues. Figure 1.1 shows a schematic of the major components in the primary and secondary circuits of a PWR [7]. The main types of light water reactors involve the boiling water reactor (BWR), and pressurized water reactor (PWR), along the heavy water reactor that was developed in Canada by CANDU (CANadian Deuterium Uranium); these types of water cooled

reactors all operate at relatively high temperature (~300°C), with high stress (PWR: 15MPa, BWR: 7MPa), companied by chemically aggressive coolant (water containing boric acid and LiOH), and experience high neutron flux radiation (10^{13} n/cm^2/s (> 0.1 MeV)).

For generation IV fission and fusion energy systems that have been proposed and are under various stages of research and development, there are five key radiation degradation effects, including low temperature radiation hardening and embrittlement, radiation-induced and -modified solute segregation and phase stability, irradiation creep, void swelling and high-temperature helium embrittlement. Figure 1.2 shows a schematic illustration of the advanced fusion reactor ARIES-AT under development. The coolant from blanket outlet temperature can be as high as 1000°C. The neutron flux is anticipated at a level of about 10^{14}n/cm^2/s, with an energy spectrum peaked at 14MeV.

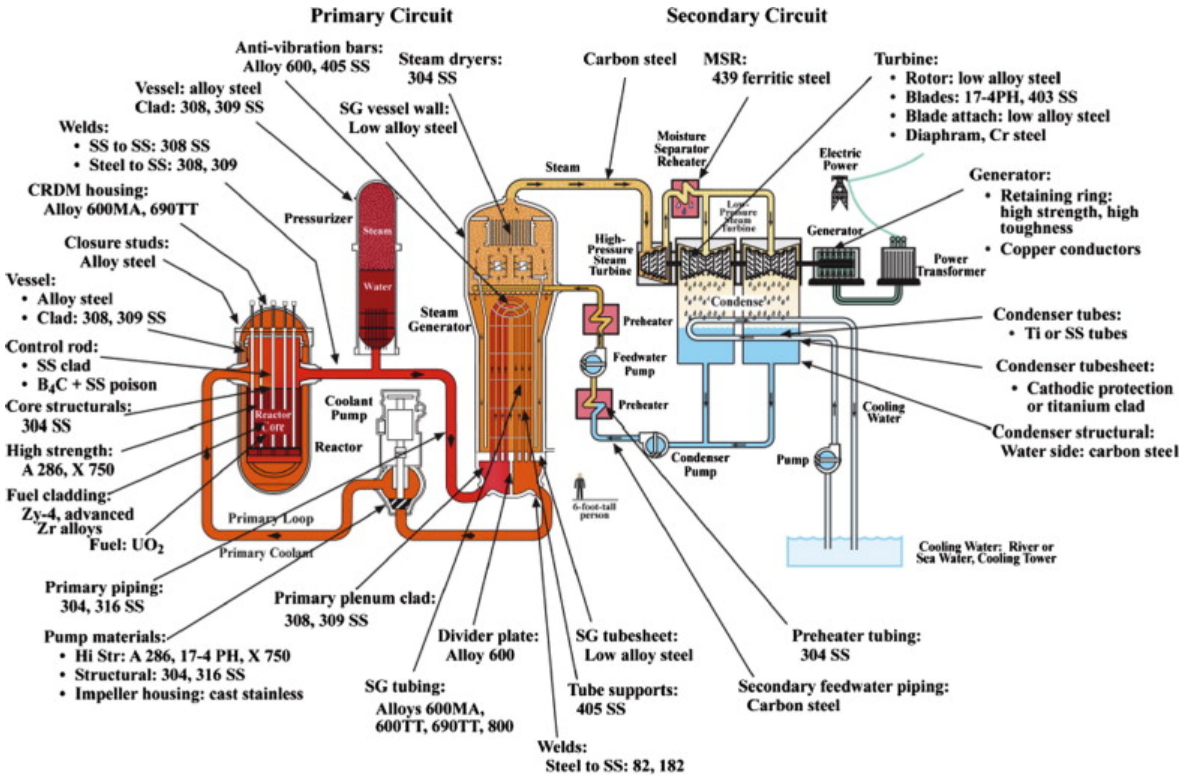

Figure 1.1 Schematic of the primary and secondary circuits of a pressurized water reactor and materials of construction [7]

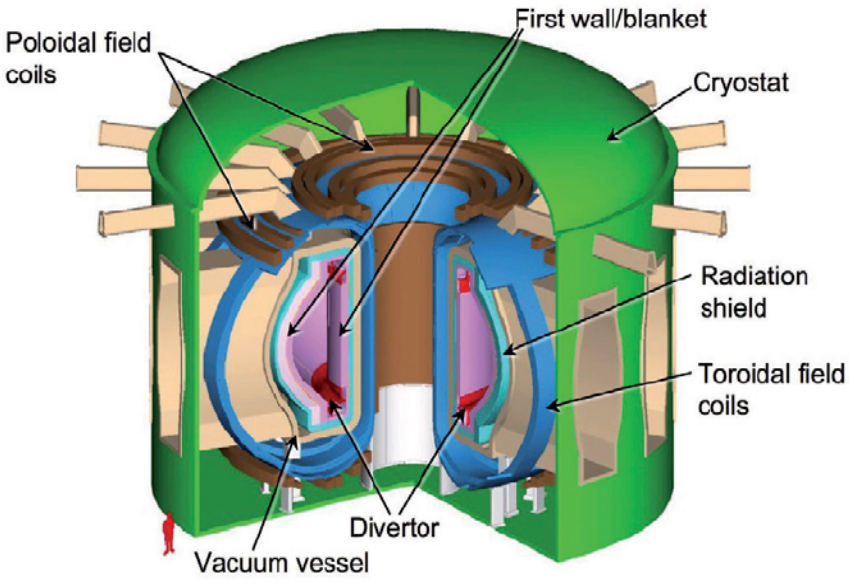

Figure 1.2 The ARIES-AT fusion power core [8]

1.2 Radiation damage processes

1.2.1 Radiation damage event

The radiation damage event is defined as the transfer of energy from an incident projectile to an atom within the solid, and the resulting collisional re-distribution of target atoms after completion of the event. This process contains several successive generations of atomic collisions during its evolution. After the interaction of an energetic incident particle with a lattice atom, energy is transferred to the lattice atom that is often significantly larger than the binding energy of the atom in the solid, which gives birth to a primary knock-on atom (PKA). The displaced PKA travels in its passage through the lattice, undergoing electronic and nuclear interactions and collisions, which can produce additional knock-on atoms, and which is typically referred to as a displacement cascade. The event concludes as the PKA comes to rest, along with the production of highly non-equilibrium concentrations of point defects (vacancies and interstitials) and clusters of these defects in the crystal lattice [9].

1.2.2 Irradiation effects on structure materials

Exposure to neutrons degrades the mechanical performance of structural materials and impacts the economics and safety of current and future fission power plants as a result of the following phenomena, which are dependent on the irradiation temperature. Low temperature radiation hardening and embrittlement/decreased uniform elongation, are observed to occur in a temperature range up to ~ 0.4 T_m, where T_m is the melting temperature in Kelvin. Irradiation and thermal creep are usually observed for temperatures below and above 0.45 T_m, respectively. In the intermediate temperature range from 0.3 to 0.6 T_m, phase instabilities driven by radiation-induced segregation and radiation-enhanced diffusion and precipitation along with dimensional instabilities driven by volumetric swelling are the key concerns. As well, high temperature He embrittlement of grain boundaries can cause intergranular fracture at low stresses, particularly for doses > 10 dpa (He concentrations > 100 appm) and temperatures above 0.5 T_m [5].

1.3 Helium induced materials degradation

Helium will be generated in the structural materials due to nuclear (n,α)-reactions during neutron irradiation or due to direct helium implantation, concurrently with high density of displacement defects.

As a noble gas atom, He has several unique characteristics, the most notable of which is an extremely low solubility in most metallic materials. It has a high potential to combine with defects such as interstitials, vacancies and their clusters, as well as extended defects such as dislocations, grain boundaries, and cavities or precipitate interfaces [10]. He bubbles formed in the grains or along the grain boundaries can result in swelling, significant radiation hardening or degradation in creep rupture behavior, and can further result in premature failure of the materials under relatively low stress [11-12].

Figure 1.3 shows a representative example of helium impact on mechanical properties specifically focused on creep rupture, and shows that as the helium concentration increase in the material the creep rupture time decreases significantly [13]. Data on the impact of helium tend to indicate a threshold at a few hundred appm where

the helium effects become very much pronounced. Nucleation of helium bubbles around microstructure defects can trigger dimensional swelling resulting in mechanical property degradation of stainless steel, as shown in Table 1.1[14]. Not only how much helium is generated in the material is important, but also how the initial microstructure involving defect clusters, precipitates and extended defect evolution due to radiation damage influences how the helium behaves and its impact on swelling, remain unanswered questions. This is evident with the 20% cold worked sample, in which the increase in initial dislocation line density in the material resulted in much less swelling than the solution treated alloy. Again, this provides a hint that the interaction between defects microstructure including lines dislocation with helium can influence the helium bubble nucleation and impact the transition from helium bubble to voids that cause a void-swelling based dimensional change.

1.4 Motivation

In order to eventually develop predictive capabilities of materials performance in the harsh nuclear fusion environment, it is extremely important to reveal the fundamental mechanisms of helium-defect interactions, which are needed to provide insight to the helium bubble nucleation and growth and the resulting materials degradation.

In this study, a coordinated experimental and modeling investigation on the influence of radiation damage on He behavior has been performed, focusing on the enhanced helium clustering in Fe and neutron irradiation impacts on the thermal helium desorption spectra.

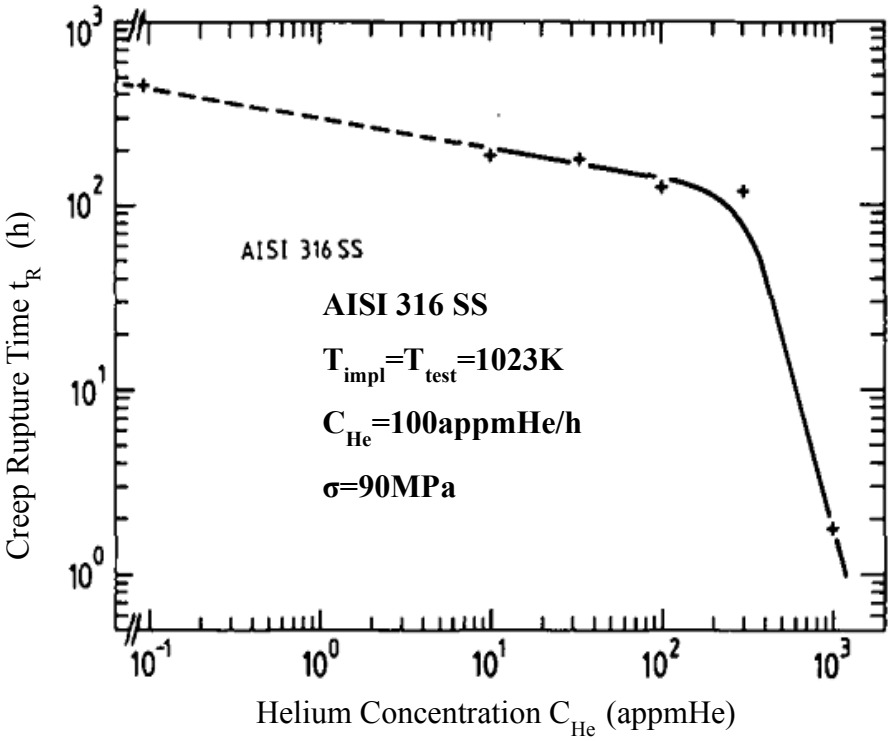

Figure 1.3 Influence of the helium concentration (pre-implanted at 1023K) on the creep rupture properties of AISI 316 SS[13]

Table 1 Irradiation Conditions and Measured Swelling for Type 316 Stainless Steel Irradiated in the HFIR [14]

Specimen position	Irradiation Temperature (℃)	Displacement (dpa)	Helium Content (appm)	Measured Swelling, %	
				Solution Treated	20% Cold worked
4	379	97	4020	6.7	1.6
5	456	107	4820	8.7	0.8
6	528	114	5450	8.3	2.6

Chapter 2

Research Approach

2.1 Molecular Dynamics (MD) Simulation

2.1.1 Introduction

Excellent instrumentation exists to observe defect clusters in materials using mature materials science characterization techniques such as transmission electron microscopy (TEM), X-ray scattering, small angle neutron scattering and positron annihilation spectroscopy. But these instruments are unable to either image many of the smallest, individual defects or capture the process of cascade. Correspondingly, computer simulations, such as MD simulation, is a good way to gain a better understanding of the spatial and temporal development of the cascade as well as to observe the defect evolution dynamics of atomic-level phenomena [10]. By using the analytical interatomic potentials, which describes the force between atoms depending on the distance, and appropriate initial and boundary conditions, the process of performing an atomistic MD simulation will be fully described.

The simplified schematic of the molecular dynamics (MD) algorithm is described in Figure 2.1 [15]. First, a suitable time step is chosen (usually very small $5 - 10\times10^{-15}$s) and atoms are provided with an initial position $r_0$and velocity v_0. Based on the selection of an appropriate potential, the forces on all atoms can be obtained by by using $F = -\nabla V(r_0)$ or $F = F(\psi(r_0))$, and then Newton's equations of motion can be integrated such that the acceleration, $a = F/m$. Applied boundary conditions such as temperature and pressure control as needed to calculate and output physical quantities of interest, as the equations of motion are integrated for each atom using a predictor-corrector. Following each integration step, the time step is moved forward $t = t + \Delta t$ and, all positions and velocities are updated for the next iteration. This procedure continues until a termination condition is reached.

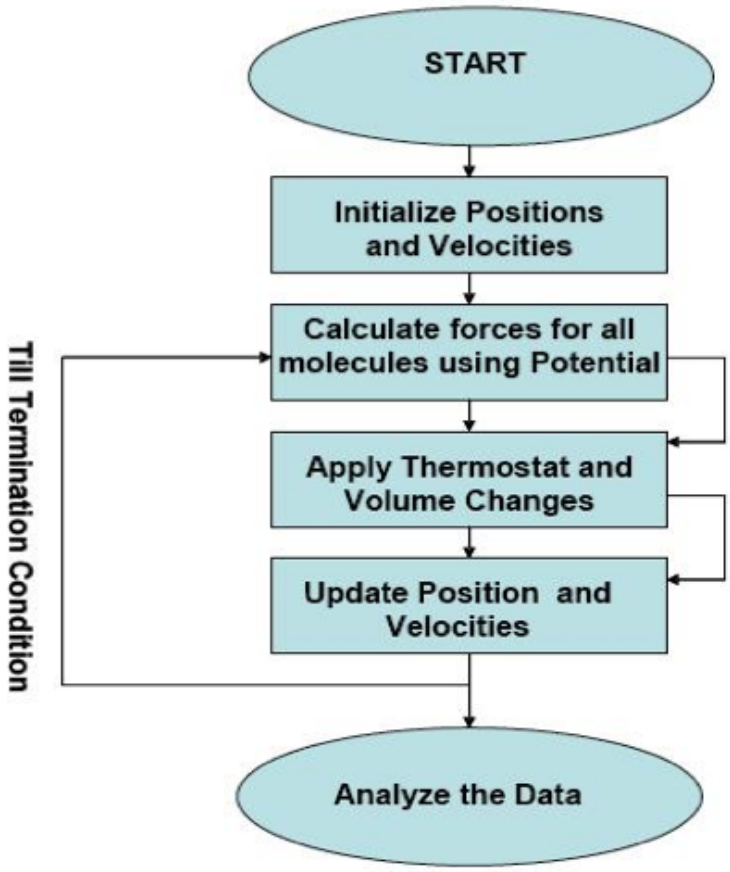

Figure 2.1 Flow chart describing the logic for a molecular dynamics simulation [15]

2.1.2 MD simulation set-up

He-point defect interaction in Fe has been widely studied by using both MD simulation and ab initio modeling. In order to reveal the fundamental mechanisms of helium behavior in Fe-based alloys, MD simulations are used to investigate the synergistic interactions of helium and prismatic dislocation loops in modifying the helium clustering and gas bubble nucleation process in BCC iron.

The simulations that have been performed involve three conditions, two of which included prismatic dislocation loops with one additional simulation condition without a pre-existing defect to provide a control simulation for comparison. In particular, a self-interstitial cluster of about 318 atoms was initially created with a prismatic dislocation loop morphology and a Burgers vector of either a<100> or a/2<111>. All of the MD simulations were performed at two different working temperatures of 500°C or 900°C. The simulation box, which is shown in Figure 2.2, has a size of $80a_0 \times 80a_0 \times 80a_0$, where a_0 refers to lattice parameter ($a_0 = 2.8654$Å). Periodic boundary conditions are applied in all three directions. In order to make it easier to create the dislocation loop in the <111> direction (along the x-axis), the crystal simulation cell was re-oriented. The LAMMPS code used to create the initial prismatic interstitial loop is presented in the Appendix.

One helium atom is randomly introduced into the modeling box every 5ps, equivalent to an insertion rate of 2×10^{11} appm He/s, up to an ultimate concentration of 2500 appm He. It is important to point out that this insertion rate is many orders of magnitude larger than expected in a real fusion environment, in which the anticipated He production rate in iron is $\sim10^{-5}$ appm/s. However, this is to accelerate the helium clustering phenomena to a timescale amenable to observation during these MD simulations. We have also selected the higher temperature simulation to further accelerate the helium diffusion, and to influence the helium clustering kinetics as a first step towards compensation for the higher implantation rate.

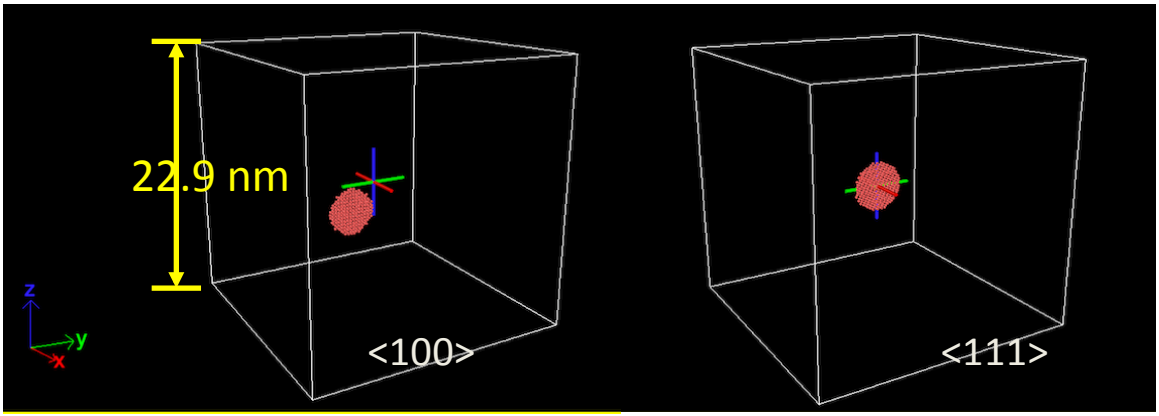

Figure 2.2 Initial condition of the simulation box

2.2 Interatomic Potentials

2.2.1 Introduction

Interatomic potentials are used to describe the forces between two atoms, atom to ion or ion to ion, which is governed by interactions between electron clouds, the electron cloud and nucleus, and between nuclei. The function is complicated and strongly depends on the atom energies and the distance of closet approach of their nuclei. Figure 2.3 shows a general overview of the variation of interatomic potential with separation r [10]. At a long distance, two atoms are interacting with each other by the simply described by Coulomb forces and the central repulsion dominates at a small distance. At the distance r_e where the two forces go to equilibrium reaching the lowest potential. To be specific, Figure 2.4 shows the behavior of various potential functions over a range of separation distances between copper atoms. When the distance between two atoms is $a_0 < r < r_e$, the electronic interactions dominates and the most accurate potential to describe this is Born-Mayer potential. Here a_0 is the Bohr radius of the hydrogen ($a_0 = 0.053nm$), r_e is the closest spacing in the crystal neighbors (~ 0.25nm). While the atoms are approaching, the electron cloud around the nuclei becomes overlap to the other, then the potential to describe this is known as screened Coulomb potential. While $r \ll a_0$, Coulomb interactions dominate.

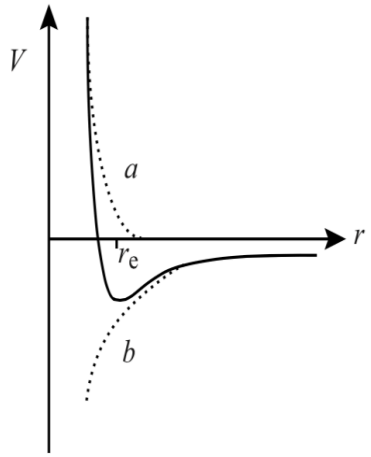

Figure 2.3 Schematic plot of interatomic potential as a function of the distance between atoms, r [10]

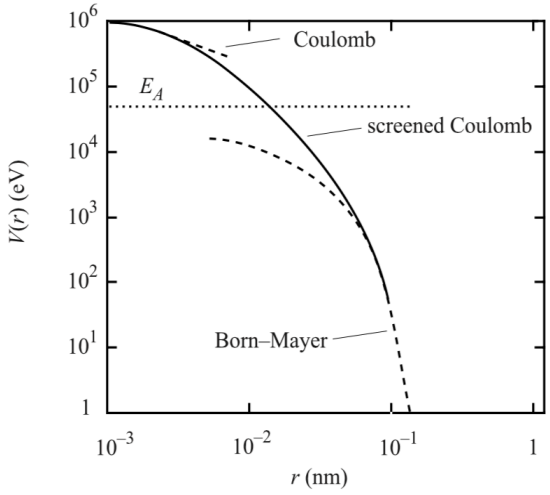

Figure 2.4 Schematic plot of interatomic potential as a function of the distance between atoms r [10]

2.2.2 Potentials used in this work

The He-He is the lightest van der Waals system and it is almost dominated by dispersion energy. Jazen's potential, which is based on modified Tang-Toennies model, provides a more reliable standard for helium viscosity [17]. The mathematical representation of the potential is as follow:

$$V(R) = A\exp(-\alpha R + \beta R^2) - \frac{\left[1-\left(\sum_{k=0}^{6}\frac{(\delta R)^k}{k!}\right)\times \exp(-\delta R)\right]C_6 f(R)}{R^6} - \sum_{n=4}^{8}\left[1-\left(\sum_{k=0}^{2n}\frac{(\delta R)^k}{k!}\right)\exp(-\delta R)\right]C_{2n}/R^{2n} \quad (1)$$

where R is the atomic separation in units of Bohr.

The Fe-Fe potential was developed by Ackland [18], incorporating both ab inito and experimental data. The potential is written is the form of an embedded atom method formalism, such that: (2)

$$U = \sum_i F_i\left[\sum_j \phi(r_{ij})\right] + \sum_{ij} V(r_{ij})$$

The He-Fe potential was developed and modified by using the density-function theory (DFT) with the DMol97 program package [19]. It has been specifically fit to incorporate the range of interaction energies of relevance for high-energy displacement atomic collisions. The specific description of this potential is:

$$f(r_{ij}) = \begin{cases} \text{DMOL} - \text{potential}\,, & r_{ij} \le r_1 \\ p_3 r_{ij}^3 + p_2 r_{ij}^2 + p_1 r_{ij} + p_0, & r_1 \le r_{ij} \le r_2 \\ \left(a + \frac{b}{r_{ij}}\right)e^{c r_{ij}} f_c(r_{ij}), & r_{ij} \ge r_2 \end{cases} \quad (3)$$

where the cut of function $f_c$is included for computational efficiency. It is given by:

$$f_c(r_{ij}) = \begin{cases} 1, & r_{ij} \le r_c - r_d \\ \frac{1}{2}\left(1 - sin\frac{\pi(r_{ij}-r_c)}{2r_d}\right), & \left|r_c - r_{ij}\right| \le r_d \\ 0, & r_{ij} \ge r_c + r_d \end{cases} \quad (4)$$

2.3 Experimental Investigation on Helium behavior in Neutron-Irradiated Iron

High neutron flux is the main issue in the radiation damage of structural materials. During the fusion environment, ${}_1^2H + {}_1^3H = {}_2^4He + n$ is the most basic reaction. High-energy neutron (14MeV) is produced along with a high-energy alpha (helium) particle, concurrently with high density of displacement defects. Furthermore, the high neutron energy can induce nuclear transmutation reactions, which can also generate helium through (n,alpha) reactions. Helium has a strong tendency to interact with defects and to form helium bubbles, which might induce dimensional swelling or high temperature grain boundary embrittlement. Given the fact that there is no fusion-relevant neutron source in the world, it is important to utilize the currently available fission reactors to investigate the influence of neutron-irradiation induced defects on the helium behavior in Fe.

2.3.1 Thermal Desorption Spectrometry (TDS)

Thermal Desorption Spectrometry is a method of observing desorbed gas atoms or molecules from a surface when the surface temperature is increased. In this study, TDS was used to capture the impact of neutron irradiated induced damage on the helium desorption behavior. The picture of the TDS facility at ORNL is shown in Figure 2.5. The TDS has two working modes, either static or dynamic. If the pumping speed is negligible, the system operates in the static mode, and if the pumping speed is relatively high, it is called the dynamic mode of operation. In dynamic mode, the helium desorption rate is approximately proportional to the detected helium number in the system by the mass spectrometer [5].

The working principle is pretty straightforward. First, the sample is implanted by 10 keV helium to a fluence of $7\times10^{14}\ He/cm^2$ at room temperature in the implantation chamber by using a 20 keV ion gun, which is operating in a raster scanning mode with a

raster area of 3.5 mm × 3.5 mm. Then the implanted sample placed in a tungsten crucible is transferred to the heating chamber by using a magnetically coupled transporter. After reaching a vacuum level of $< 2\times10^{-9}$ torr, the temperature of the sample is increased to 1150°C with a ramping rate of 0.5°C/s. In the temperature ramping process, helium will be thermally dissociated from the original He-defect complex and then desorbed out of the sample surface, depending on the binding energies. Then the released helium will be captured and measured by a quadrupole mass spectrometer in the measurement chamber. Figure 2.6 shows the principle of a TDS procedure when probing He-point defect interaction.

2.3.2 Transmission Electron Microscopy (TEM)

Due to the limitation of the resolution in light microscopy, which is imposed by the wavelength of visible light, Transmission Electron Microscopy (TEM) is a more widely used technique to observe the nano-scale microstructure by using electron beams accelerated at high voltage with effective wavelengths that are shorter by a factor of 10^5 than visible light. It is a microscopy technique in which a beam of electrons is transmitted through an ultra-thin specimen, interacting with the specimen as it passes through it. TEM has many limitations in practical, such as samples must be thin, dry, and capable of scattering electrons in a vacuum [20]. However, it is still the most powerful tool to investigate the microstructural evolution of materials subject to irradiation. In this study, TEM was used to characterize the dislocation loops and voids in neutron-irradiated single crystalline and polycrystalline iron.

Microstructure characterization of the irradiated samples were conducted in low activation materials development and analysis lab (LAMDA) at ORNL by using transmission electron microscopy (TEM, JEOL JEM 2100F), of which the samples were prepared by using focus ion beam (FIB, FEI Quanta 3D DualBeam).

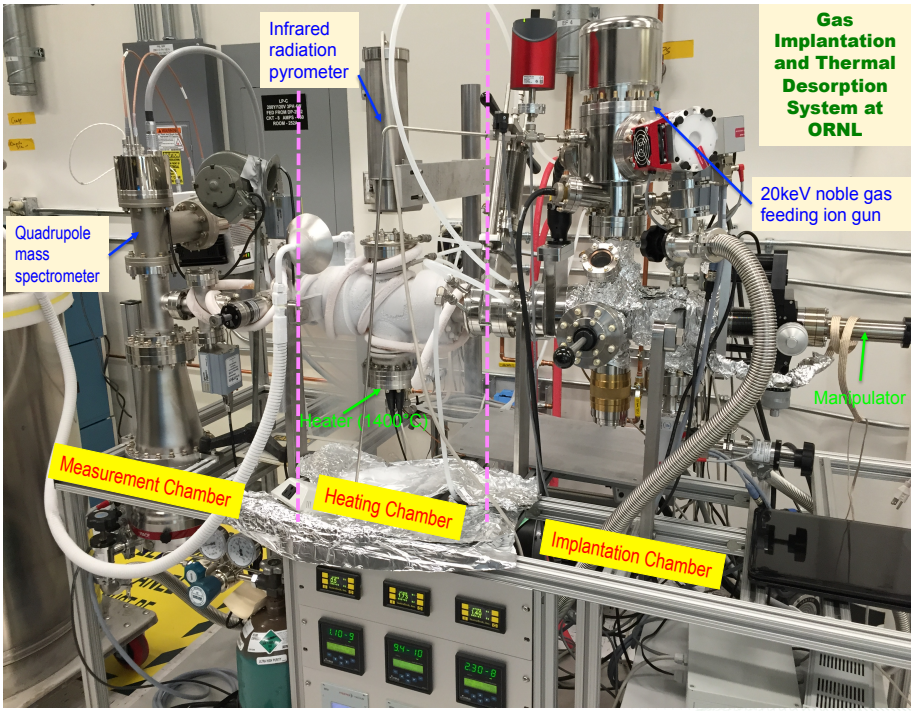

Figure 2.5 TDS facility at ORNL

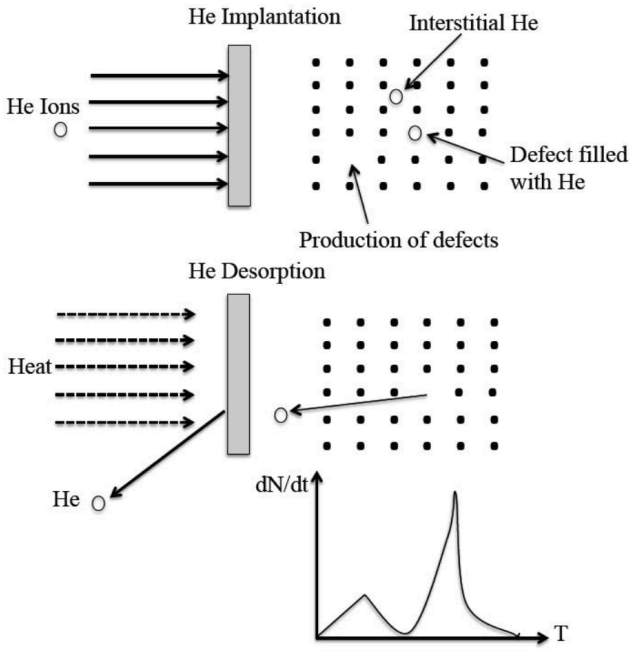

Figure 2.6 The principle of a TDS procedure when probing He-point defect interaction [5]

Chapter 3

Simulation Results and Discussion

In this Chapter, the results from MD simulations were present. The three specific simulation conditions of helium implantation into the iron simulation cell are: these including an initial a<100> loop, or an a/2<111> loop or without a prismatic loop present, and all of the MD simulations were performed at either 500°C or 900°C. The first specific question to be answered is how the helium clustering or helium bubble nucleation processes are modified based on the presence of the prismatic dislocation loop, as well as the temperature dependence. Subsequently, how the existence of helium will affect the behavior of defects is discussed.

3.1 Helium clustering process at 500°C

Figures 3.1, 3.2 and 3.3 show the helium clustering process observed during the MD simulations of the three different loop conditions, namely with <100>, with <111> and without a pre-existing loop, respectively. In these Figures, the red ball represents iron atom and blue ball represent helium atom, respectively. A helium cluster is defined in this thesis as more than two atoms sticking together. As the helium insertion continues, helium clusters begin to accumulate, and as these clusters grow in size, the interstitial helium clusters eventually build sufficient pressure to induce the formation of a Frenkel pair on the body centered cubic iron lattice in a process referred to as trap mutation. Once trap mutation occurs, the helium cluster moves onto the vacancy and the iron self-interstitial atoms stay in the vicinity of the helium clusters, until eventually diffusing to an extended defect cluster where they can be annihilated through absorption. From Figure 3.1 and Figure 3.2, when 500 appm He is inserted, it's clear to see helium first start to accumulate around the periphery of the loop, and the loop also grows in size by absorbing the interstitials around it. Meanwhile, a large amount of helium and iron clusters can also observed in the area far away from the loop center.

Comparing the simulations with and without the pre-existing loop, it is clear that for these simulation conditions the existence of the loop does not have a significant

influence on the helium clustering process. Figure 3.4 shows a statistical analysis, which compares the concentration of cluster and monomer density, and which shows that the clustering process is slightly slower without the loop. But until the final stage of the simulation (2500 appm He), the presence of an a/2<111> loop in the box promotes the most helium cluster density.

3.2 Helium clustering process at 900℃

The helium insertion process at 900℃ is shown in Figures 3.5 to 3.8. Helium and iron interstitial clusters have again been observed, and the dislocation loops also grow by absorbing the iron interstitials, all of which are generally similar to the observations from the MD simulations at 500℃. However, a lower number density and bigger size of helium cluster were observed at the higher temperature.

Figure 3.8 shows that at 900°C, the dislocation loop has a much more significant influence on the helium bubble nucleation compared to the lower temperature of 500°C. The monomer concentration is much higher for non-loop condition before decreasing as the helium clusters begin to form. Especially at the initial stage of the insertion procedure, the helium cluster concentration is much higher than the two with-loop cases. As the end of the simulation is approached with a helium concentration of 2500 appm, it is also evident that the presence of the a/2<111> loop promotes more helium clusters than the other two cases.

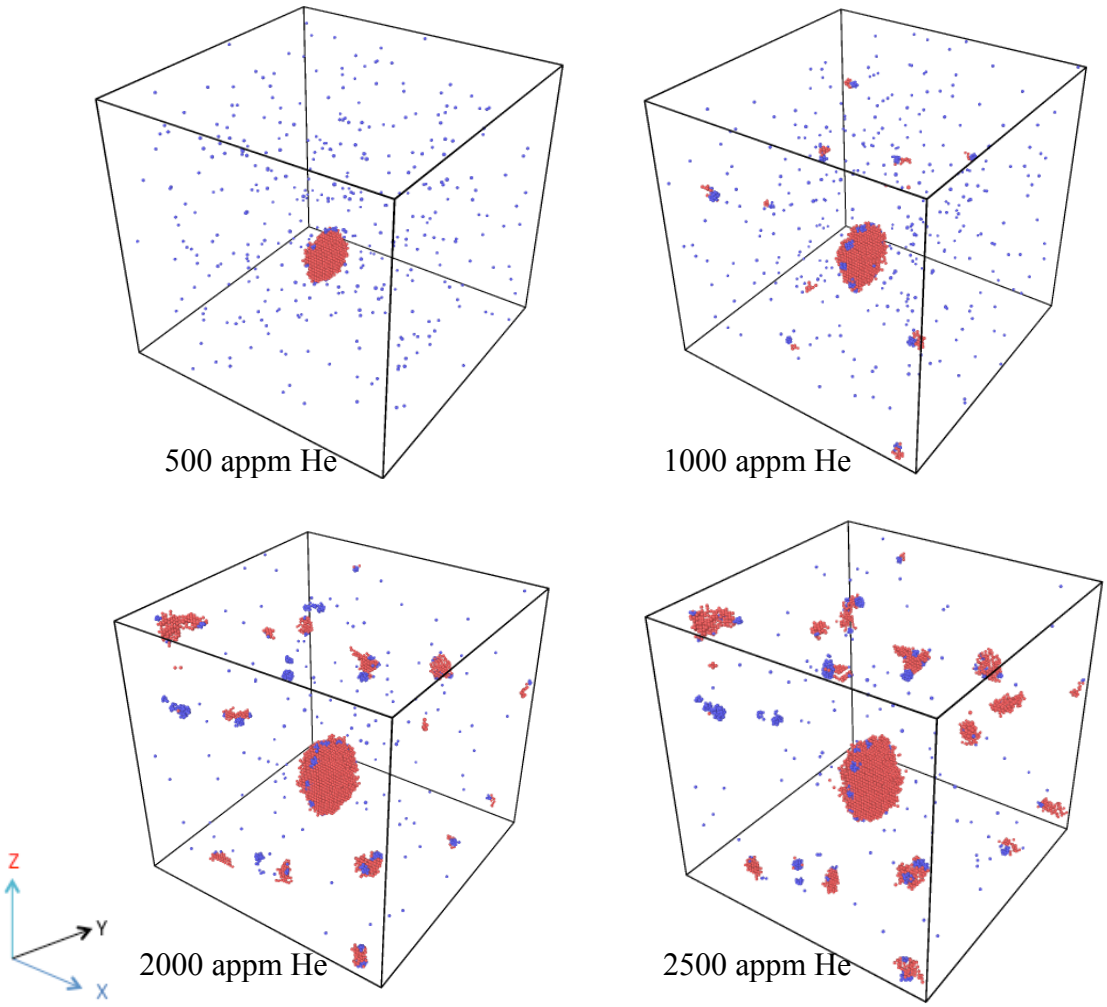

Figure 3.1 Helium clustering process at 500°C, loop<100>

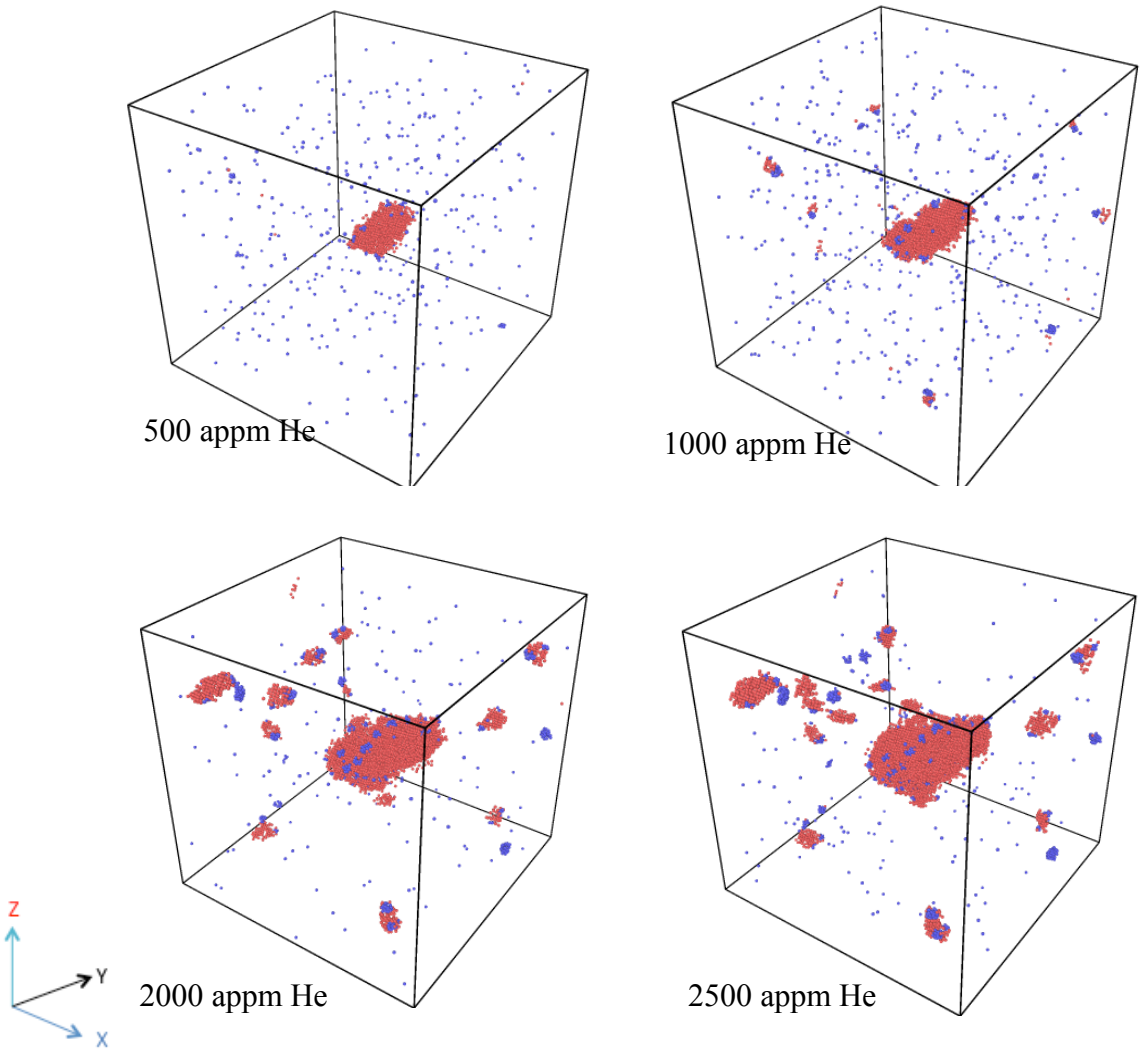

Figure 3.2 Helium clustering process at 500°C, loop<111>

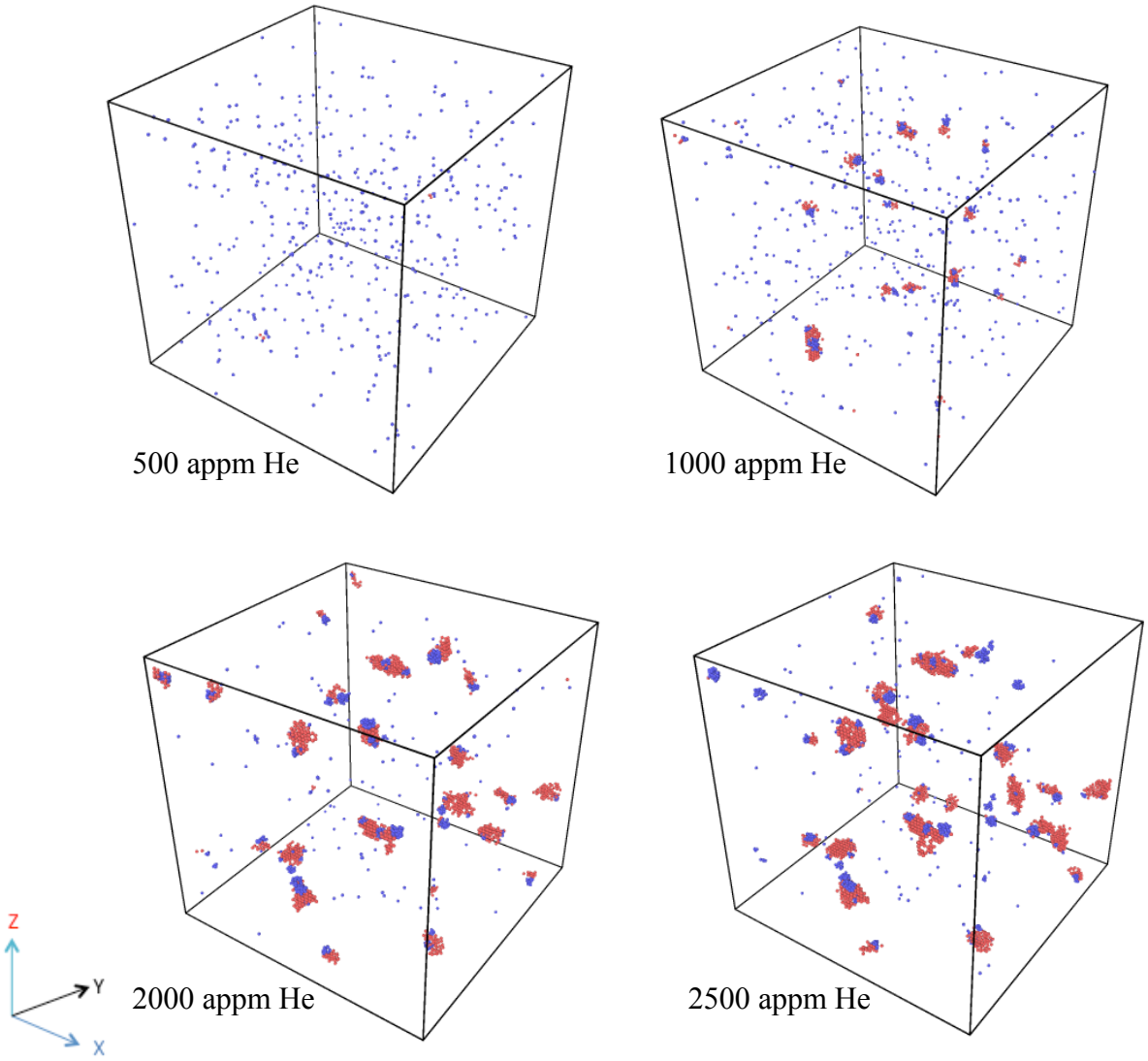

Figure 3.3 Helium clustering process at 500°C, without a pre-existing loop

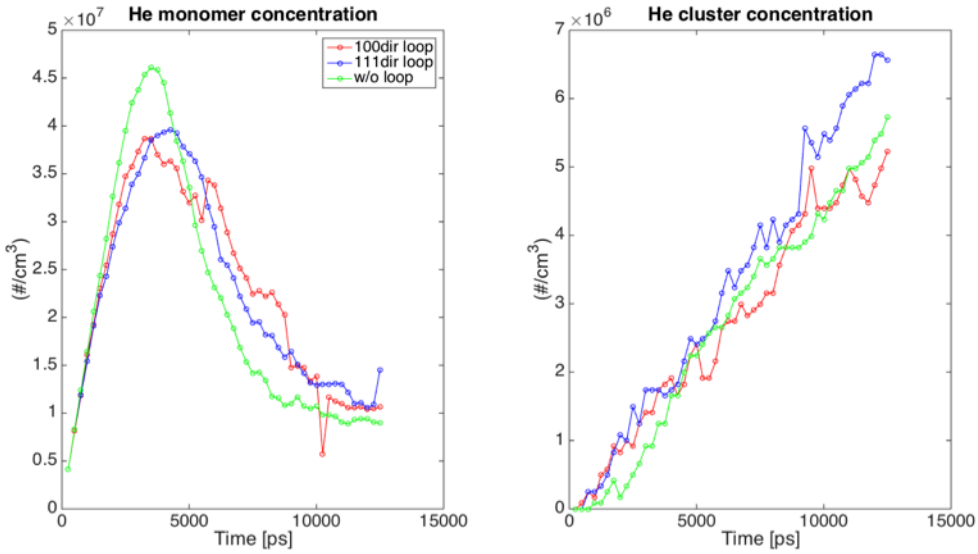

Figure 3.4 Comparison of He cluster & monomer concentration at 500°C

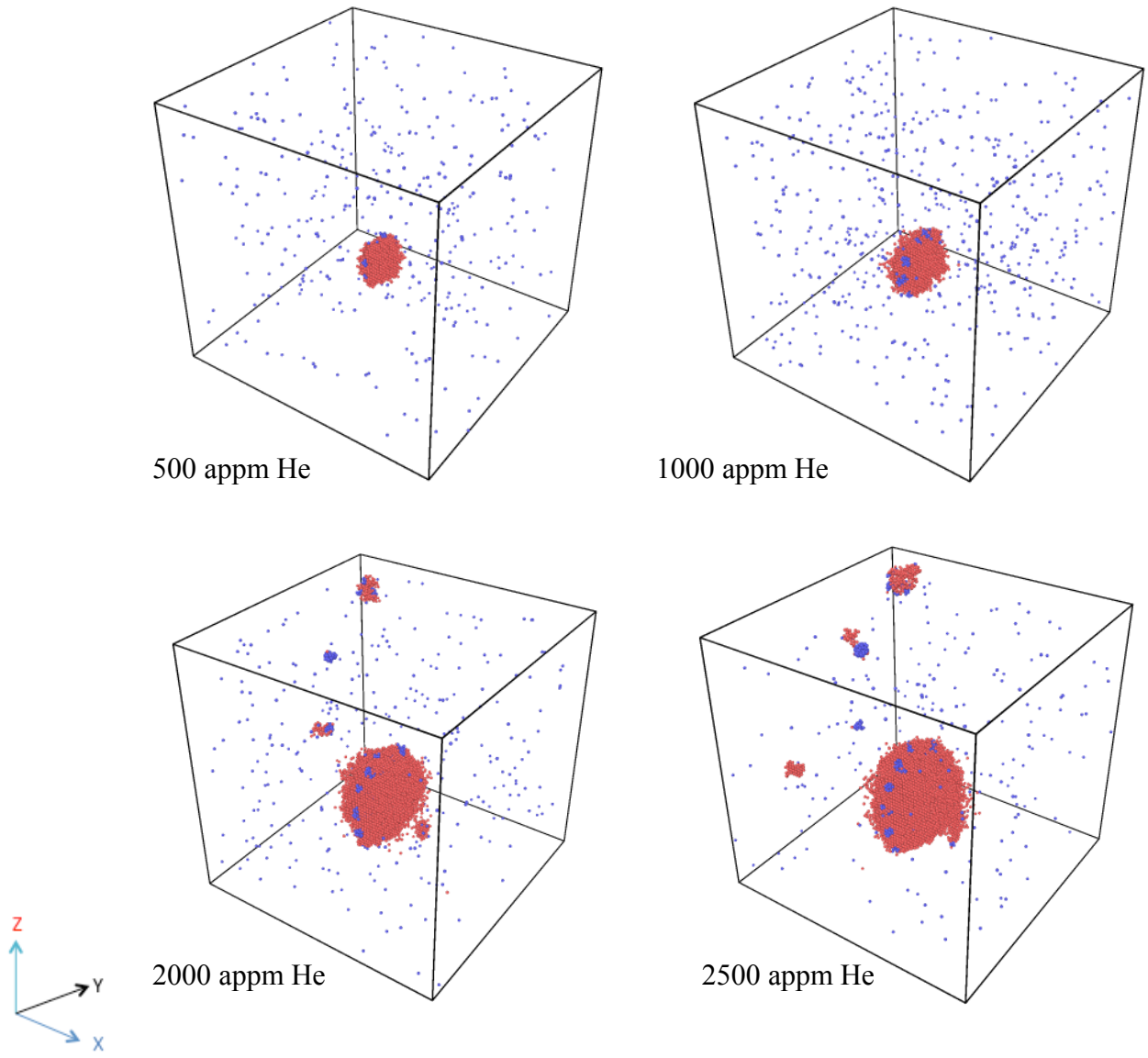

Figure 3.5 Helium clustering process at 900°C, loop<100>

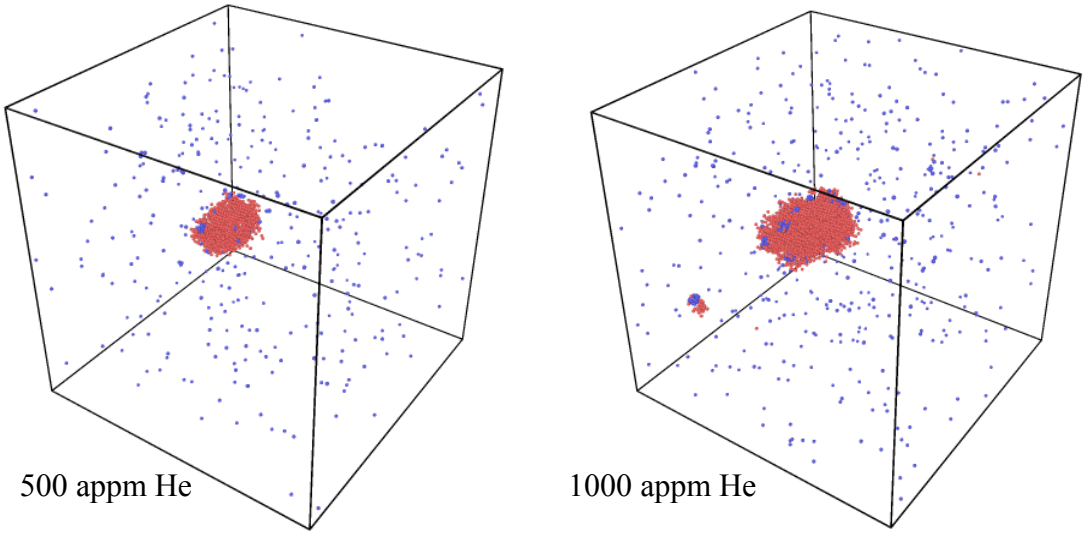

Figure 3.6 Helium clustering process at 900°C, loop<111>

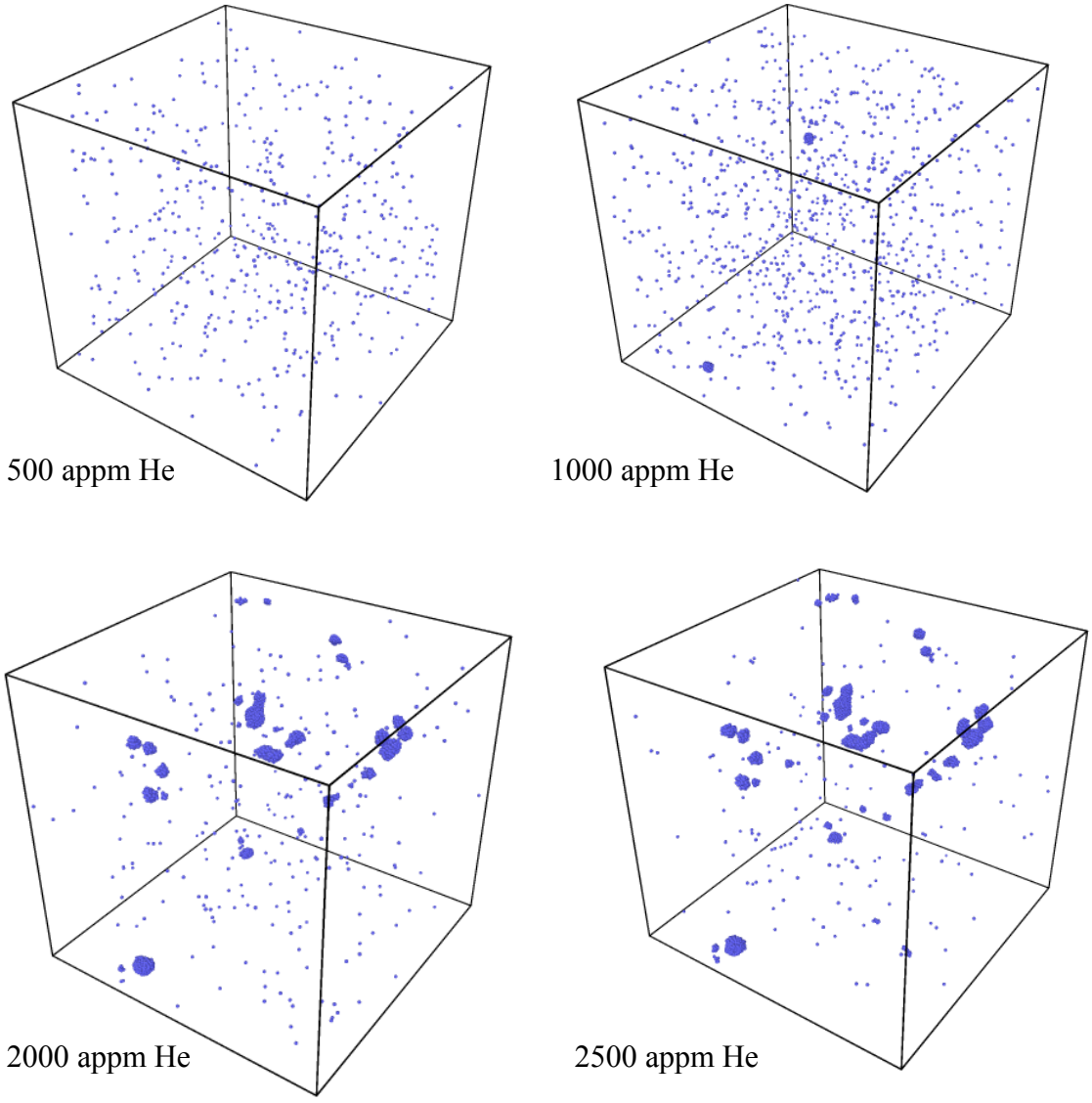

Figure 3.7 Helium clustering process at 900°C, without a pre-existing loop

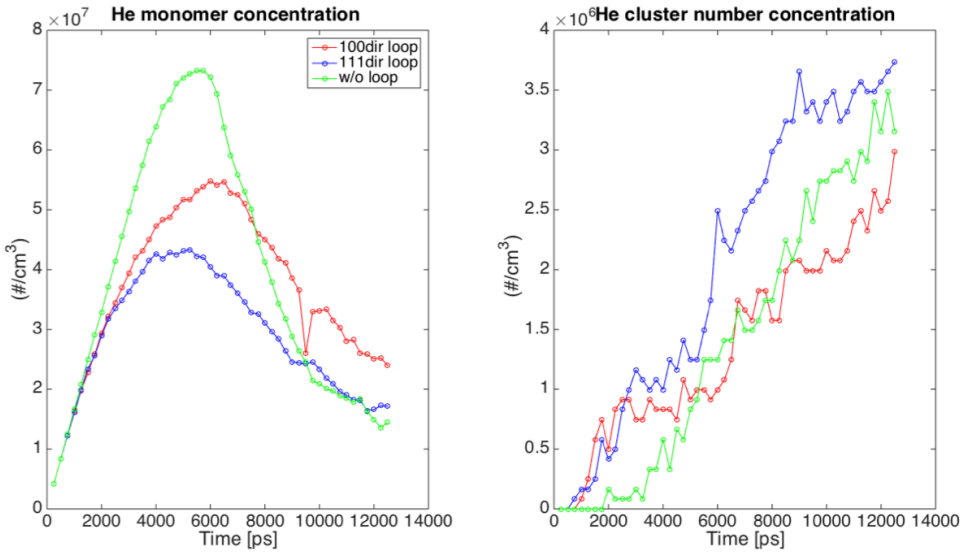

Figure 3.8 Comparison of He cluster & monomer concentration at 900°C

3.3 He clusters distribution at a concentration of 2500 appm He

The helium cluster size distribution is shown in Figure 3.9. As described previously, at higher temperature, the He cluster size distribution covers a much broader region while at lower temperature, the majority of He exists in small clusters. The presence of the a/2<111>dislocation loop promotes the clustering of He more significantly, compared to the other two cases.

3.4 Temperature dependence of He clustering

To investigate the temperature dependence of the helium clustering, Figure 3.10 shows the helium distribution from the MD simulation with or without a prismatic loop with Burgers vector of a<100>, where to aid the visualization, the loop is not explicitly imaged. However, it is clear in Figure 3.10, that a number of helium bubbles clearly form in the periphery of the loop location. At the higher temperature of 900°C, the helium cluster size is bigger and the number density is smaller. For these cases of the a<100> loop, it is again clear that the initial helium cluster nucleation occurs near the periphery of the dislocation loop.

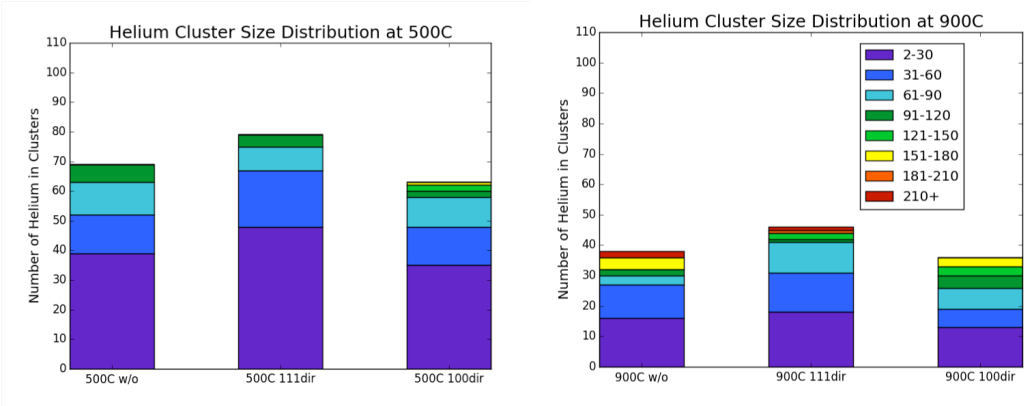

Figure 3.9 Helium clusters distribution at a concentration of 2500 appm He

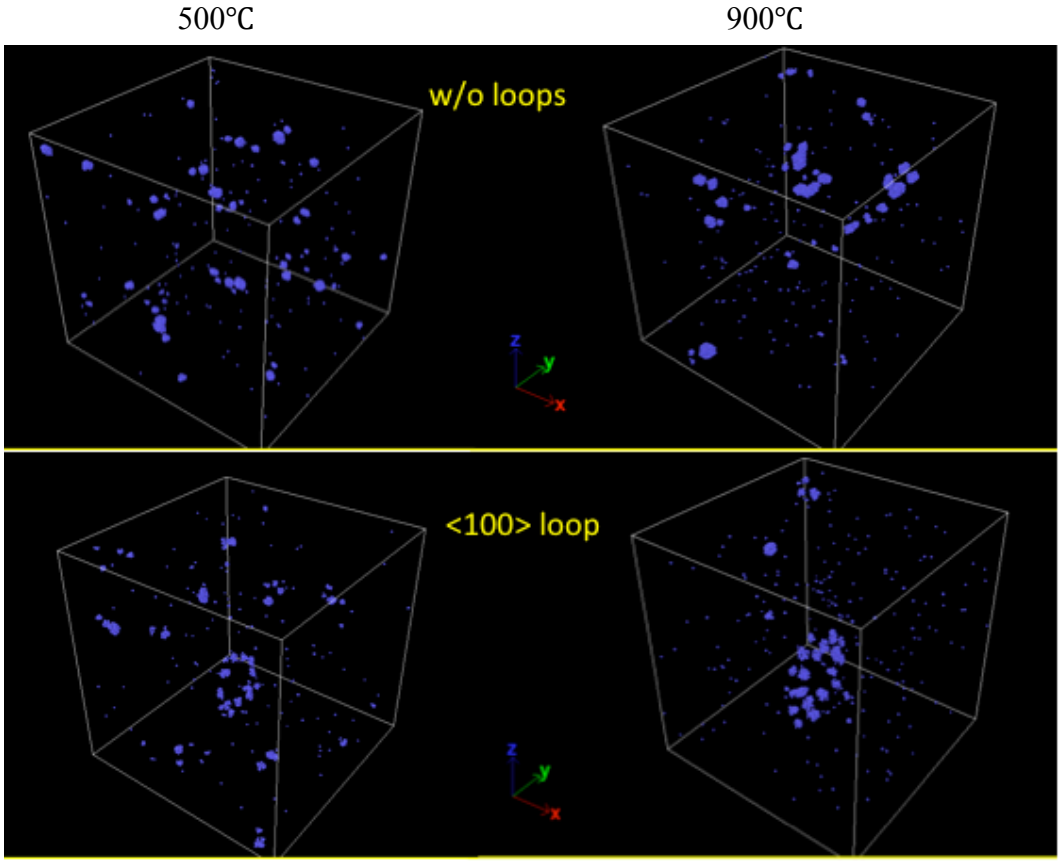

Figure 3.10 Temperature dependence of helium clustering process

3.5 Dislocation loop size comparison

As described in previous content, the pre-existing dislocation loop will grow by absorbing the iron interstitials produced by increasing pressure in the box. During the process of helium insertion, the size of the loop was measured every 500 ps, equivalent to a rate at 10 appm He. The diameter of the loop was averaged by four directions' measurement, horizontal, vertical and deviation form vertical by $\pm 45°$. The loop size growing process is shown in Figure 3.11.

According to the statistic analysis, the <100> loop turns to have a huge dependence on temperature, the great divide happens after around 1000 appm He where higher temperature promotes bigger loop growth. While in the <111>loop simulation condition, there is limited temperature dependence. The reason of this phenomenon is still under investigation. More simulations of <100> loop are running for future analysis to exclude random error.

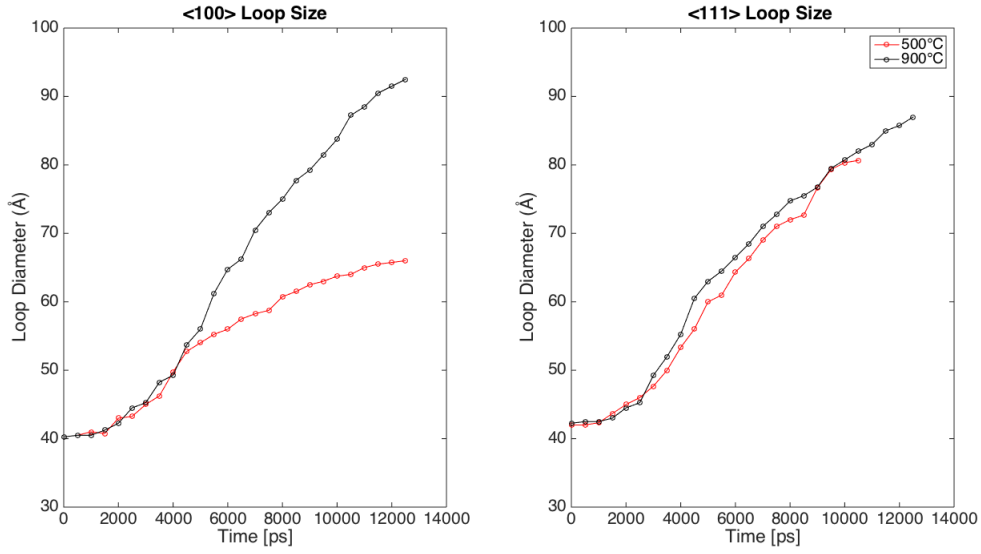

Figure 3.11 Dislocation loop size comparison

Chapter 4

Experimental Results and Discussion

Both single crystal and polycrystalline iron samples were used to investigate the helium clustering and desorption behavior after neutron irradiation. Two types of specimens have been neutron irradiated in two different nuclear reactors. Table 2 gives an overview of the neutron irradiation of iron samples. A single crystal iron sample was neutron-irradiated in the high flux isotope reactor (HFIR) at 300°C to reach a dose of about 5 dpa, and a poly-crystal iron sample was irradiated in the BOR-60 fast reactor at a higher temperature (371~395°C) to a dose of 16 dpa. The damage rates of these two irradiation conditions are $9x10^{-7}$ and $6\sim7x10^{-7}$ dpa/s, respectively, for HFIR and BOR-60 irradiation. Appropriate non-irradiated iron samples were used to provide a control to isolate the change in helium desorption resulting from the neutron irradiation.

4.1 TEM results

4.1.1 Microstructures of neutron-irradited single crystalline α-Fe

Figure 4.1 shows the results of transmission electron microscopy of the HFIR irradiated single crystal Fe specimen, in which a low number density of cavities is observed with a fairly narrow size distribution. No significant density of black dot type defect cluster, nor large dislocation loops were observed. Cavities are sparsely distributed within the grains, with a limited spatial correlation of the cavities to dislocation lines. From the TEM analysis performed using both over focus and under focus images, cavities appear mostly as spherical (green arrows), in which some of the cavities have some indication of truncated, or faceted, surface morphology. In addition, line dislocations are observed and no obvious dislocation loops exist.

Table 2 Overview of the neutron irradiation of iron samples

Sample ID	Materials type	Reactors	Reactor type	Irradiation Temperature (°C)	Radiation dose (dpa)
A4	Single crystalline Fe	HFIR (Flux trap facility)	Mixed neutron spectrum	300	5.0
F02	Polycrystalline Fe	BOR-60	Fast neutron spectrum	386	16.6

4.1.2 Microstructures of neutron-irradiated polycrystalline α-Fe

Figure 4.2 shows the results of transmission electron microscopy of the BOR-60 neutron irradiated specimen, which reveals the formation of a high number density of cavities, which appear to have a continuous (Gaussian) size distribution. Again, this neutron irradiated specimen does not exhibit any substantial black dot defect clusters nor large dislocation loops. We can see limited association of cavities with line dislocations (left image) and the appearance of a void denuded zone with a width of about 80-120 nm around grain boundaries (middle image). Cavities appear with a variety of shapes, including cuboidal (red arrow), truncated rectangular (blue arrows), or spheres (green arrows).

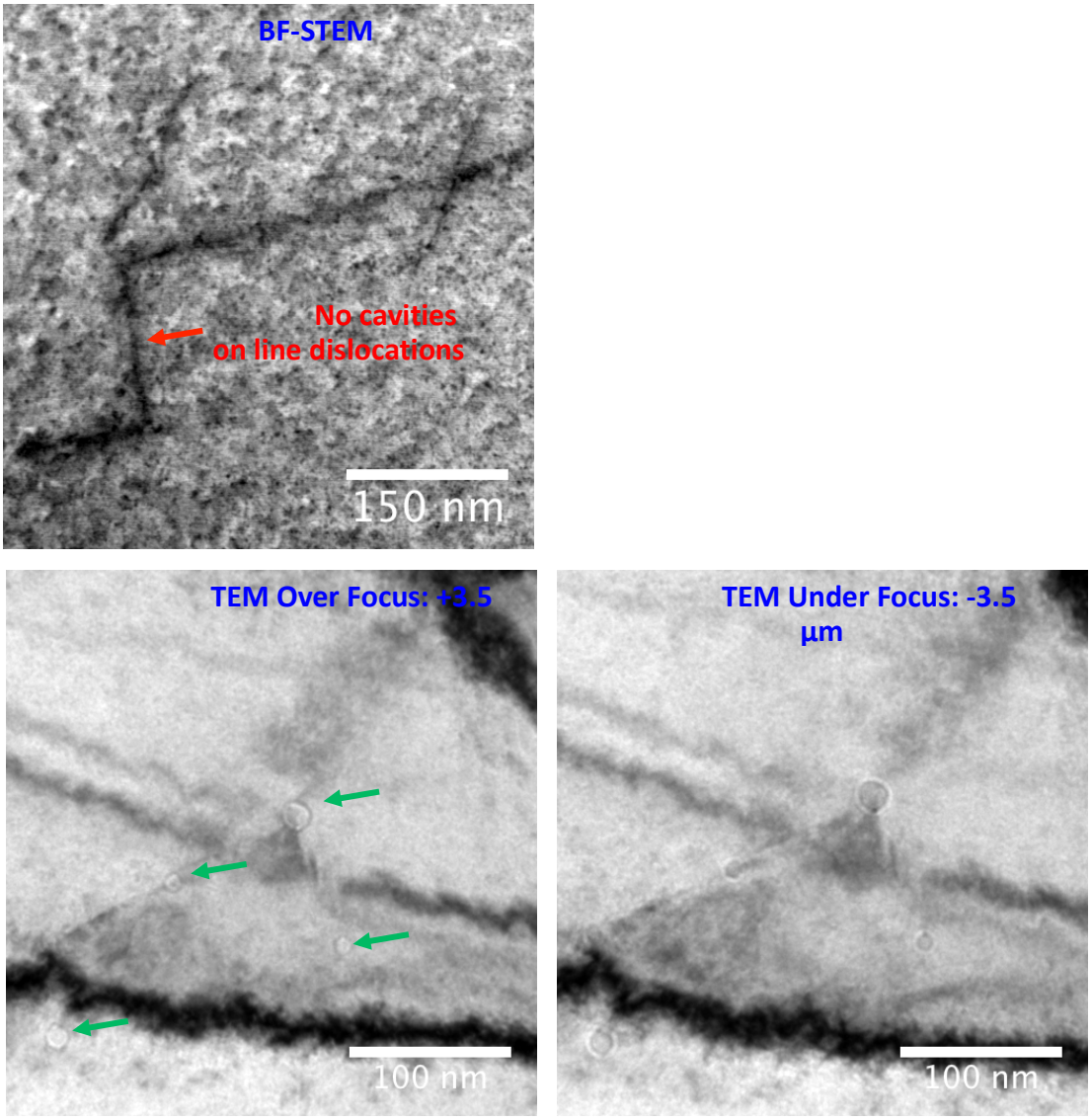

Figure 4.1 Cavity images in single crystal Fe irradiated to 5 dpa, 300°C – HFIR

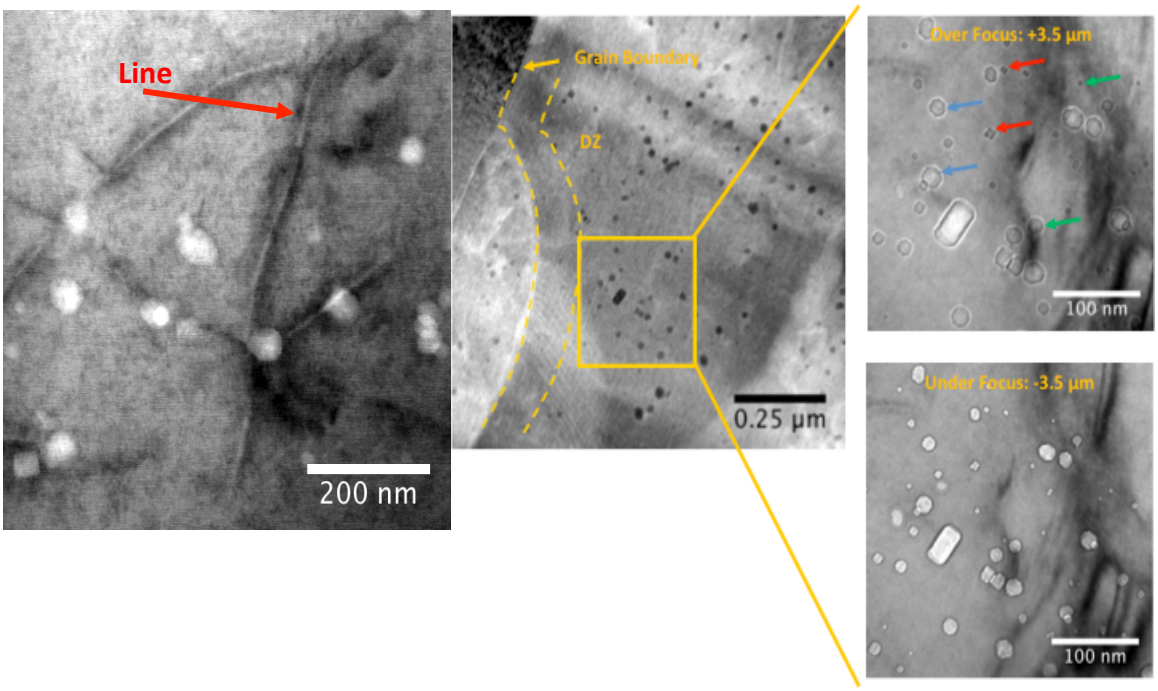

Figure 4.2 Cavity images in polycrystalline Fe irradiated to 16.6 dpa, 386°C– BOR60

4.2 Thermal Helium Desorption Spectrometry (THDS)

Figure 4.3 shows the helium desorption spectra of the non-irradiated single crystalline and polycrystalline iron samples. The left figure shows two single crystal specimens implanted with 10keV helium to a fluence of $7\times10^{14}\ He/cm^2$. The similar He desorption behaviors of these two tests imply the good repeatability of the system. The sharp He release peak at 912°C indicated the BCC-FCC transformation point, which can also be used to calibrate the measured sample temperature. The major helium desorption in BCC phase region occurs in the temperature range from 600 to 900°C, with a release peak around 750°Ç. An obvious helium desorption peak is also observed in FCC phase region, which is not complete due to the limitation of the current maximum temperature the system can reach (1150°C). The integrated release of helium during the TDS measurement is approximately 80% of the amount implanted, implying that ~ 20% of the implanted He still remain in the samples following the TDS measurement. The right-hand side plot shows the helium desorption behavior of poly-crystal iron following

the same implantation condition. Apart from the phase change peak, it is observed that the major helium release peak in the BCC region shifts to a lower temperature region, from 500 to 620°C peaked at 580°C, which is also much sharper compared to that of single crystalline Fe. This release peak may result from several mechanisms, including helium interaction and binding with impurities in the sample or as a result of a relatively low binding energy between helium atoms and the grain boundaries. In the FCC phase above 912°C, another peak was observed. The total released He is 86% of the initially implanted He. For both cases, the implanted He was not completely released, indicating the existence of stable He clusters, and possibly even that helium bubbles, formed during the implantation or the TDS measurement.

Figure 4.4 presents a comparison of the desorbed helium spectra between the non-irradiated and neutron irradiated samples. For the single crystal iron samples, the helium desorption peak shifts to higher temperature in the sample exposed to neutron irradiation. As shown in the TEM image of Figure 4.1, it was observed that several types of cavities were observed, and we should certainly expect helium to be attracted to these cavities. The binding energy of helium with point defects, impurities, defect clusters and cavity will certainly vary with the defect size or type, and correspondingly we expect a wide range of possible helium binding energies. This currently makes determination of the mechanism controlling the desorption of helium from the neutron irradiated single crystal iron very difficult at this time. Future work will need to be performed to model these experiments, as well as performing additional microstructural characterization to further identify the precise defect interactions and binding energies controlling the helium release peaks.

Likewise, similar behavior was also observed for the polycrystalline iron samples. As shown in Figure 4.2, a much higher number density of cavities is produced, which will act as the trapping sites for helium atoms making it harder to be driven out through thermal desorption. However, as noted previously, the amount of desorbed helium for the BOR-60 irradiated sample was actually much larger than the amount implanted. This implies that in addition to the cavities, or gas bubbles, absorbed in the neutron irradiated specimens by TEM examination, there must also be a fairly high concentration of small

helium, or helium-vacancy, clusters that subsequently were able to diffuse to the surface and desorb during the TDS measurement. And, again, future experimental characterization and modeling will be required to specifically identify the helium – defect interactions that are responsible for the individual desorption peaks in these specimens.

Figure 4.5 presents a comparison of the desorbed helium spectra of non-irradiated and neutron irradiated samples. For the single crystal iron, after irradiation the desorption peak shifts to higher temperature. Refer to the TEM image, we see several types of cavities, to which helium might combine. The binding energy varies with the defects size or type, resulting in different desorbing stage. The neutron irradiation induced defects enhanced the combination of He to defect clusters. Similar behavior was also observed for the polycrystalline iron samples. Much higher number density of cavities is produced, which act as the trapping sites for helium atoms making it harder to be driven out through thermal desorption technology.

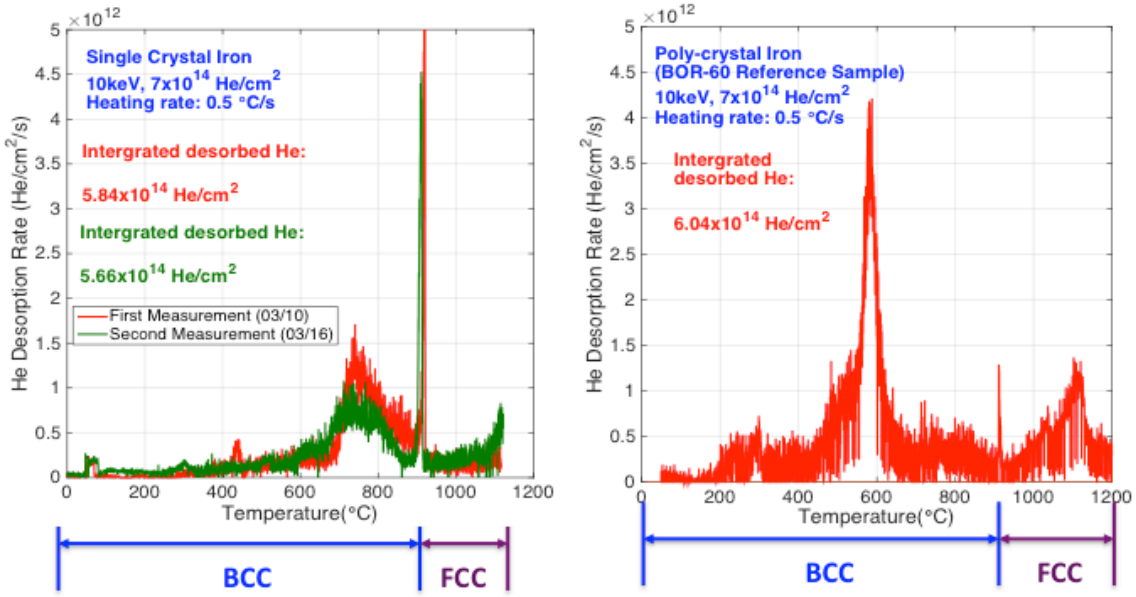

Figure 4.3 Thermal desorption spectrometry of non-irradiated Fe sample

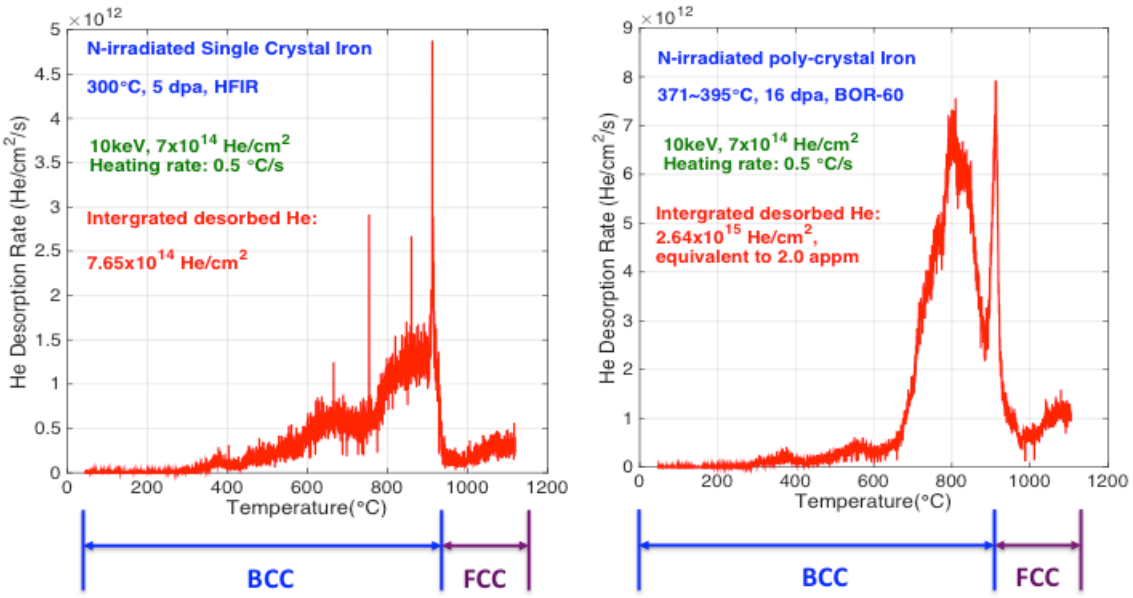

Figure 4.4 Thermal desorption spectrometry of neutron-irradiated Fe samples

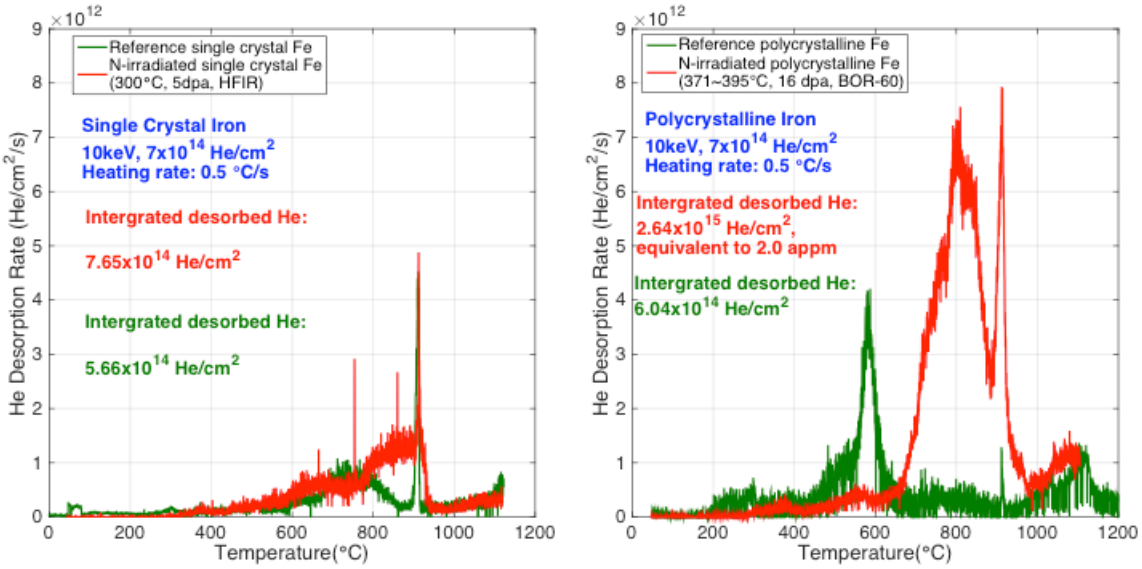

Figure 4.5 TDS comparison of non-irradiated and neutron irradiated samples

Chapter 5

Conclusions and Future Work

5.1 Summary

MD simulations have been used to investigate the influence of pre-existing prismatic dislocation loops on the helium clustering process in BCC iron. The results show that the existence of a prismatic dislocation loop at higher temperature (900℃) has a much larger influence on the initial helium clustering behavior than at lower temperature (500℃). As well, the a/2<111> dislocation loop promotes the He clustering process more significantly than a<100> loop. Both of the <111> and <100>-type dislocation loops grow in size by absorbing iron interstitials produced thru trap mutation processes as the helium clusters grow to larger size.

TEM was used to characterize the microstructure of neutron-irradiated single crystalline and polycrystalline iron. The results indicate the existence of big cavities and limited increase in the dislocation line density in both samples. We can see limited association of cavities with the line dislocations, as well as the appearance of a void denuded zone near extended defects. In the polycrystalline sample irradiated in a fast neutron spectrum in the BOR-60 reactor, a larger number of cavities with a more continuous size distribution to larger sizes was observed. In contrast, the single crystal iron specimen irradiated in HFIR, a lower density of cavities was observed, and these cavities were sparsely distributed within the grains.

TDS was used to capture the impact of neutron irradiated induced damage on the helium desorption behavior. The results show that the helium desorption spectrum shifts to higher temperature due to the strong binding of helium and the defects. A very sharp helium release peak was observed in every sample at 912℃, where the iron undergoes a phase change from BCC to FCC. During the thermal desorption process, not all of the inserted helium was released, indicating the existence of stable He bubbles formed during the implantation or the TDS heat treatment. However, for the polycrystalline iron sample irradiated in the fast neutron energy spectrum of Bor-60, the integrated desorbed He is higher than the total implanted He, indicated that a fairly significant amount of helium

was generated by transmutation (n, α) reactions, and thus helium was likely in the form of very small helium clusters so that it was able to desorb during the TDS measurement.

5.2 Future work

Future effort should investigate more extensive set of molecular dynamics simulations that could the helium insertion rate, as well as to characterize more extensively the effect of temperature and pre-existing defect geometries and types. The investigation of whether the <100> loop promotes bigger loop growth is needed. As well, a combination of additional experiments and modeling is required to determine the mechanism controlling the desorption of helium from the neutron irradiated iron specimens. The binding energy of helium with point defects, impurities, defect clusters and cavity will certainly vary with the defect size or type, and correspondingly we expect a wide range of possible helium binding energies. This currently makes determination of very difficult at this time. Future work will need to be performed to model these experiments, as well as performing additional microstructural characterization to further identify the precise defect interactions and binding energies controlling the helium release peaks.

References

[1] Energy Information Administration, Washington, DC, Report DOE/EIA-0219, 2003.

[2] E.E. Bloom, S.J. Zinkle, F.W. Wiffen, *Materials to deliver the promise of fusion power – progress and challenges*, J. Nucl. Mater. 329-333 (2004) 12-19.

[3] IAEA, *International Status and Prospects for Nuclear Power 2012*, Board of Governors General Conference, GOV/INF/2012/12-GC (56) /INF/6.

[4] Committee on America's Energy Future, *America's Energy Future: Technology and Transformation*. National Academies Press, Washington (2009).

[5] Hu (2013), *Gas Diffusion in Metals: Fundamental Study of Helium-Point Defect Interactions in Iron and Kinetics of Hydrogen Desorption from Zirconium Hydride* (Doctor dissertation). University of California, Berkeley, CA.

[6] *Introduction to the Grand Challenges for Engineering*, http://www.engineeringchallenges. org/cms/8996/9221. aspx, 2008.

[7] S.J. Zinkle, *Fusion materials science: overview of challenges and recent progress*. Phys. Plasmas 12 (2005) 058101.

[8] Farrokh Najmabadi, the ARIES Team, *The ARIES-AT advanced tokamak, Advanced technology fusion power plant,* Fusion Engineering and Design, Volume 80, Issues 1–4, January 2006, Pages 3–23

[9] Was, G. S. (2007). *Fundamentals of radiation materials science: Metals and alloys*. Berlin: Springer.

[10] E.V. Kornelsen, *The interaction of injected helium with lattice defects in a tungsten crystal.* Radiat. Eff. 13 (1972) 227–236.

[11] L.K. Mansur and W.A. Coghlan, *Mechnisms of helium interaction with radiation effects in metals and alloys: A review*. J. Nucl. Mater. 119 (1983) 1–25.

[12] H. Trinkaus, *Energetics and formation kinetics of helium bubbles in metals*, Radiat. Eff. 78 (1983) 189 – 211.

[13] Herbert Schoeder et al., *Helium Effects on the Creep and Fatigue Resistance of Austenitic Stainless Steels at High Temperatures,* Nuclear Engineering and Design/Fusion 2 (1985) 65-95

[14] F.W. Wiffen, E. E. Bloom, *Effect of High helium Content on Stainless-Steel Swelling,* Nuclear Technology 25 113 (1975)

[15] Nathan Allen Capps, *Molecular Dynamics Simulation of Cascade Evolution near Pre-Existing Defects (Master's thesis).* University of Tennessee, Knoxville, TN.

[16] Janzen, A. R., & Aziz, R. A. (1997). *An accurate potential energy curve for helium based on ab initio calculations*. The Journal of Chemical Physics J. Chem. Phys., 107(3), 914. doi:10.1063/1.474444

[17] G. J. Ackland, M. I. Mendelev, D. J. Srolovitz, S. Han and A. V. Barashev, *Development of an interatomic potential for phosphorus impurities in α-iron,* J. Phys.: Condens. Matter 16 (2004) S2629–S2642

[18] N. Juslin, K. Nordlund, *Pair potential for Fe–He*, J. of Nucl. Materials 382 (2008) 143–146

[19] Williams, D. B., & Carter, C. B. (1996). *Transmission electron microscopy: A textbook for materials science*. New York: Plenum Press.

Appendix

<111> loop box code

```
units metal
dimension 3
boundary p p p

atom_modify map array
variable lattice equal 2.8654
variable WN equal 46
variable LN equal 57
variable HN equal 33

variable W equal sqrt(3)*${lattice}*${WN}
variable L equal sqrt(2)*${lattice}*${LN}
variable H equal sqrt(6)*${lattice}*${HN}

units metal
atom_style atomic
lattice bcc ${lattice} orient x 1 1 1 orient y 1 -1 0 orient z 1 1 -2 origin 0.001 0.001 0.001

region main block 0.0 $W 0.0 $L 0.0 $H units box

variable plane_1x equal 0.5*$W
variable plane_1y equal 0.5*$L
variable plane_1z equal 0.5*$H

variable plane_2x equal 0.5*$W+0.5*sqrt(3)*${lattice}
variable plane_2y equal 0.5*$L
variable plane_2z equal 0.5*$H

variable sphere_x equal 0.5*$W
variable sphere_y equal 0.5*$L
variable sphere_z equal 0.5*$H

variable radius equal 7.5*${lattice}

region habitplane1 plane ${plane_1x} ${plane_1y} ${plane_1z} 1 0 0 units box
region habitplane2 plane ${plane_2x} ${plane_2y} ${plane_2z} -1 0 0 units box
region spheredisloc sphere ${sphere_x} ${sphere_y} ${sphere_z} ${radius} units box
region extra intersect 4 main habitplane1 habitplane2 spheredisloc

create_box 2 main
create_atoms 1 region extra
group loop region extra
```

```
variable b_displ equal 0.25*${lattice}*sqrt(3)
displace_atoms loop move ${b_displ} 0 0 units box
create_atoms 1 region main

mass 1 55.847
mass 2 4.0026

# Force Fields
pair_style hybrid table linear 10000 eam/fs
pair_coeff * * eam/fs /lustre/home/zhuang18/newton/potential/Fe-Ackland2004.eam.fs
Fe NULL
pair_coeff 1 2 table /lustre/home/zhuang18/newton/potential/FeHe-Juslin2008.table FeHe
pair_coeff 2 2 table /lustre/home/zhuang18/newton/potential/He-Janzen1997.table He

minimize 0 0 10000 10000

dump 1 all atom 1000 minimized.all
dump 2 loop atom 1000 minimized.loop

timestep 0.001

velocity all create 1543.0 25232351 dist gaussian
thermo_style custom step temp pe etotal press vol lx ly lz
thermo 1000
thermo_modify lost error
fix 1 all nvt temp 773.0 773.0 1
thermo 100

run 1000
unfix 1
```

<100> box loop code

```
units metal
dimension 3
boundary p p p
variable lattice equal 2.8654
atom_modify map array


variable l_x equal 80*${lattice}
variable l_y equal 80*${lattice}
variable l_z equal 80*${lattice}

variable z_thick equal 1.5*${lattice}
variable z_W_max equal ${l_z}+0.01*${lattice}
variable z_W_min equal -0.01*${lattice}

variable plane_1x equal 39.9*${lattice}
variable plane_1y equal 39.0*${lattice}
variable plane_1z equal 32.0*${lattice}

variable plane_2x equal 40.6*${lattice}
variable plane_2y equal 39.0*${lattice}
variable plane_2z equal 32.0*${lattice}

variable sphere_x equal 40.25*${lattice}
variable sphere_y equal 32.0*${lattice}
variable sphere_z equal 32.0*${lattice}
variable radius equal 7.1*${lattice}

region habitplane1 plane ${plane_1x} ${plane_1y} ${plane_1z} 1 0 0
region habitplane2 plane ${plane_2x} ${plane_2y} ${plane_2z}  -1 0 0
region boundary sphere ${sphere_x} ${sphere_y} ${sphere_z} ${radius}

region simbox block 0 ${l_x} 0 ${l_y} 0 ${l_z}
create_box 2 simbox
region dislocate intersect 4 simbox habitplane1 habitplane2 boundary

lattice bcc ${lattice}
create_atoms 1 region dislocate
group loop region dislocate
displace_atoms loop move 0.5 0 0
create_atoms 1 region simbox
mass 1 55.847
mass 2 4.0026
```

```
# Force Fields

pair_style hybrid table linear 10000 eam/fs
pair_coeff * * eam/fs /lustre/home/zhuang18/newton/potential/Fe-Ackland2004.eam.fs
Fe NULL
pair_coeff 1 2 table /lustre/home/zhuang18/newton/potential/FeHe-Juslin2008.table FeHe
pair_coeff 2 2 table /lustre/home/zhuang18/newton/potential/He-Janzen1997.table He

minimize 0 0 10000 10000

dump 1 all atom 1 dump.boxloop100_500C.all
dump 2 loop atom 1 dump.boxloop100_500C

timestep 0.001

velocity all create 1543.0 25232351 dist gaussian
thermo_style custom step temp pe etotal press vol lx ly lz
thermo 1000
thermo_modify lost error
fix 1 all nvt temp 773.0 773.0 0.1
thermo 100
run 1000
```

Vita

Zuya Huang was born in Chongqing, China to the parents of Yazhou Huang and Hong Cao. She went to Nankai middle school got her high school graduation certificate in 2010. Then she attended North China Electric Power University at Beijing where she earned the bachelor of Science degree in Nuclear Science and technology in June of 2014. She accepted a Graduate Research Assistant position within the Nuclear Engineering Department at the University of Tennessee upon graduation in 2014. Zuya will earn a Master of Science degree in Nuclear Engineering in May of 2016.